

GOTCHA Experience Report: Three-Dimensional SAR Imaging with Complete Circular Apertures

Emre Ertin, Christian D. Austin, Samir Sharma, Randolph L. Moses and Lee C. Potter

The Ohio State University
Department of Electrical and Computer Engineering
2015 Neil Avenue, Columbus, OH 43210

ABSTRACT

We study circular synthetic aperture radar (CSAR) systems collecting radar backscatter measurements over a complete circular aperture of 360 degrees. This study is motivated by the GOTCHA CSAR data collection experiment conducted by the Air Force Research Laboratory (AFRL). Circular SAR provides wide-angle information about the anisotropic reflectivity of the scattering centers in the scene, and also provides three dimensional information about the location of the scattering centers due to a non planar collection geometry. Three dimensional imaging results with *single* pass circular SAR data reveals that the 3D resolution of the system is poor due to the limited persistence of the reflectors in the scene. We present results on polarimetric processing of CSAR data and illustrate reasoning of three dimensional shape from multi-view layover using prior information about target scattering mechanisms. Next, we discuss processing of *multipass* (CSAR) data and present volumetric imaging results with IFSAR and three dimensional backprojection techniques on the GOTCHA data set. We observe that the volumetric imaging with GOTCHA data is degraded by aliasing and high sidelobes due to nonlinear flightpaths and sparse and unequal sampling in elevation. We conclude with a model based technique that resolves target features and enhances the volumetric imagery by extrapolating the phase history data using the estimated model.

Keywords: Synthetic Aperture Radar, Three Dimensional Imaging, Circular SAR, Polarimetric Processing, Wide-angle Imaging

1. INTRODUCTION

In this paper, we consider processing of SAR data collected on multiple complete circular apertures. Our study of this data collection scenario is motivated by the GOTCHA CSAR data collection experiment conducted by the Air Force Research Laboratory (AFRL).¹ This publicly released data set contains eight complete circular passes collected at an altitude of 25,000 feet and 45 degree elevation angle using an airborne fully polarimetric SAR sensor. The circular aperture and the elevation diversity enables construction of volumetric three dimensional imagery from the collected backscatter data.

Imaging with circular SAR systems and with the traditional isotropic point source assumption have been previously considered.^{2,3} The point scattering model assumes the scattering center amplitude is independent of frequency and aspect angle, with a phase term encoding the spatial location of the backscatter. While this assumption is a valid approximation for narrow apertures used by traditional radar imaging systems, empirical studies have shown that few reflectors provide persistent response larger than 20 degrees.^{4,5} Circular SAR has two unique features to its wide-angle non-planar collection geometry. First, it provides wide-angle information about the unisotropic reflectivity of the scattering centers in the scene. Second, unlike the linear collection geometry, circular SAR reveals three dimensional information about the location of the scattering centers in the spotlighted area. In this paper, we illustrate these concepts using computed examples from the GOTCHA data set and introduce new algorithms for CSAR processing for 3D target reconstruction.

The paper is organized as follows. Section 2 gives a brief overview of imaging theory with CSAR data and discusses imaging methods suited for wide-angle imaging with single pass CSAR data, and shows wide-angle images computed from a single pass of the GOTCHA data set. In Section 3 we analyze the flight paths from the volumetric passes in the GOTCHA dataset and discuss the aliasing and sidelobe structure of the system point spread function. Section 4 gives the results on polarimetric processing of GOTCHA data and illustrates

reasoning of three dimensional shape from multi-view layover using prior information about target scattering mechanisms. In Section 5 and 6 we present volumetric imaging results with IFSAR and three dimensional backprojection techniques. We show that the volumetric imaging with GOTCHA data is degraded by aliasing and high sidelobes due to nonlinear flightpaths and sparse and unequal sampling in elevation. In Section 7 we propose a model based technique that resolves target features and enhances the volumetric imagery. We conclude with future research directions.

2. IMAGING WITH CIRCULAR SAR

In this section we briefly review imaging with CSAR data.^{2,3,6} We consider the following system model for circular SAR. The SAR system collects coherent backscatter measurements $g_j(f_k)$ on circular apertures parameterized with azimuth angles $\{\phi_j\}$ covering $[0, 2\pi]$ and the elevation angle θ . The backscatter measurements are at discrete set of frequencies $\{f_k\}$. The imaging problem is to estimate the three dimensional reflectivity function of the spotlighted scene $f(x, y, z)$ from the set of radar returns $\{g_j(f_k)\}$ collected by the radar. The three dimensional version of the projection-slice theorem shows that the backscatter measurements represent samples of the 3-D spatial Fourier transform of the reflectivity function.⁷ Specifically, let $F(k_x, k_y, k_z)$ denote the 3-D Fourier transform of the reflectivity function $f(x, y, z)$:

$$F(k_x, k_y, k_z) = \int \int \int f(x, y, z) e^{-i(k_x x + k_y y + k_z z)} dx dy dz. \quad (1)$$

Then the radar measurements $\{g_j(f_k)\}$ correspond the samples of $F(k_x, k_y, k_z)$ on a two dimensional conical manifold at points $(k_x^{j,k}, k_y^{j,k}, k_z^{j,k})$:

$$k_x^{j,k} = \frac{2\pi f_k}{c} \cos(\theta) \cos(\phi_j) \quad k_y^{j,k} = \frac{2\pi f_k}{c} \cos(\theta) \sin(\phi_j) \quad k_z^{j,k} = \frac{2\pi f_k}{c} \sin(\theta) \quad (2)$$

The inverse Fourier Transform of the data calculated on the conical manifold results in the coherent wide-angle volumetric image $I(x, y, z)$. We note that any 2D slice $I(x, y, z_0)$ contain all the information from the single pass, and all 2D slices can be regenerated from the ground plane image $I(x, y, 0)$ using:

$$I(x, y, z_0) = \mathcal{F}_{(x,y)}^{-1} \left[\mathcal{F}_{(x,y)}[I(x, y, 0)] e^{-i\sqrt{k_x^2 + k_y^2} \tan(\theta) z_0} \right] \quad (3)$$

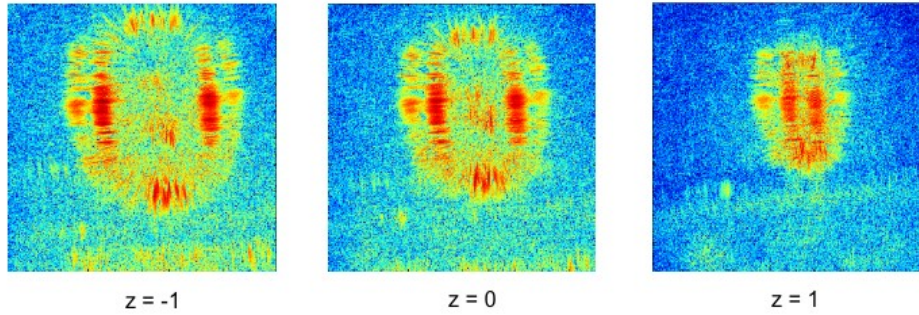


Figure 1. Two dimensional slices $I(x, y, z)$ from the volumetric CSAR image at three different heights

Images for a vehicle calculated from the GOTCHA set at three different heights are shown in Figure 1. We observe that the 3D resolution of CSAR images with data collected from a *single pass* is poor due to limited persistence of the target reflectors, with reflectors appearing focused at all three heights. Using Cramer-Rao bound analysis, Moore and Potter⁸ showed that height resolution comparable to range resolution can only be obtained for reflectors with persistence greater than $\pi/4$. We note that the wide-angle coherent image $I(x, y, 0)$

is not an efficient data representation for the radar returns, because it requires a high spatial sampling rate to prevent aliasing of the circular bandpass signature given by:

$$\delta_x < \frac{c}{4\cos(\theta)(f_c + \text{BW}/2)} \quad (4)$$

This Nyquist sampling rate for the GOTCHA data is 1.07 centimeters. Also wide-angle coherent imaging is matched to isotropic point reflector assumption. Instead, for CSAR data processing we adopt image sequences $\{I_m(x, y, 0)\}_m$ where each image is the output of a filter matched to a limited-persistence reflector over the azimuth angles in window $\mathcal{W}_m(\theta)$. Specifically, the m-th subaperture image is constructed using

$$I_m(x, y, 0) = \mathcal{F}_{(x,y)}^{-1} \left[F(k_x, k_y, \sqrt{k_x^2 + k_y^2} \tan(\theta)) \mathcal{W}_m(\tan^{-1}(k_x/k_y)) \right] \quad (5)$$

where the azimuthal window function $\mathcal{W}_m(\phi)$ is defined as:

$$\mathcal{W}_m(\phi) = \begin{cases} W\left(\frac{\phi - \phi_m}{\Delta}\right), & -\Delta/2 < \phi < \Delta/2 \\ 0, & \text{otherwise} \end{cases} \quad (6)$$

θ_m is the center azimuth angle for the m-th window and Δ describes the hypothesized persistence width. The window function $W(\cdot)$ is an invertible tapered window used for cross-range sidelobe reduction. We also note that unlike the full 360 degree image, each image can be modulated to baseband and sampled at a lower resolution without causing aliasing. Each baseband image $I_m^B(x, y, z)$ is calculated as:

$$I_m^B(x, y, 0) = I_m(x, y, 0) e^{-j(k_x^0 + k_y^0)}. \quad (7)$$

where the center frequency (k_x^0, k_y^0) is determined by the center aperture θ_m , mean elevation angle θ and center frequency f_c .

$$k_x^0 = \frac{2\pi f_c}{c} \cos(\theta) \cos(\phi_c), \quad k_y^0 = \frac{2\pi f_c}{c} \cos(\theta) \sin(\phi_c). \quad (8)$$

For small azimuth windows Δ , the Nyquist sampling rate for each image $I_m^B(x, y, 0)$ is dictated by the radar bandwidth and results in much smaller storage requirement for CSAR data. The image sequence $\{I_m(x, y, 0)\}_m$ can be enhanced by deconvolving the subaperture point spread function⁹ and can be visualized in many different ways. One possibility is to use GLRT imaging proposed by Moses and Potter.¹⁰ The GLRT image $I_G(x, y, z)$ can be obtained by taking a non-coherent maximum over the sub-aperture imagery:

$$I_G(x, y, z) = \max_m |I_m^B(x, y, z)| \quad (9)$$

Figure 2 shows the enhanced GLRT image for a vehicle from the GOTCHA set where the color in each pixel denotes the subaperture index for which the maximum return occurs.

3. THE GOTCHA DATASET

The GOTCHA data set is fully polarimetric and consists of eight complete circular (360°) passes, with each pass being at a different elevation angle, θ ; the radar used in the GOTCHA data collection has a center frequency of 9.6 GHz, giving a center wavelength of $\lambda_c = 0.031$, and a bandwidth of 640 MHz. Each pass has a planned (ideal) separation of $\Delta\theta = 0.18^\circ$ in elevation with a planned elevation $\theta \in [43.7^\circ, 45.0^\circ]$. Actual flight paths differ from the planned paths, with elevation varying as a function of azimuth angle. Table 1 shows planned elevation angles of each of the 8 passes and the mean elevation angle of each of the actual passes. Figure 3 shows the eight passes in a global coordinate system, where the z dimension is height as measured from the ground plane in meters. This figure demonstrates the change in elevation angle across each pass.

By using the multiple passes at different elevation angles, standard tomographic imaging methods, such as polar reformatting or backprojection, can be applied in to reconstruct 3D images of the scene. Resolution and aliasing in the height dimension of a reconstruction coordinate system is governed by the same equations as used in the azimuth direction. Defining the height dimension with respect the slant plane coordinate system as z_S ,

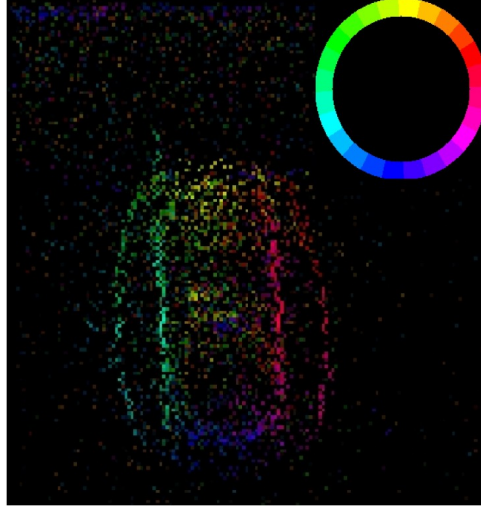


Figure 2. Enhanced GLRT image, the color denotes the subaperture index with the maximum radar return

Pass	Planned (Ideal) Elevation (degrees)	Mean Actual Elevation (degrees)
1	45	45.66
2	44.82	44.01
3	44.64	43.92
4	44.45	44.18
5	44.27	44.14
6	44.08	43.53
7	43.89	43.01
8	43.71	43.06

Table 1. Planned and mean elevation angle of 8 passes

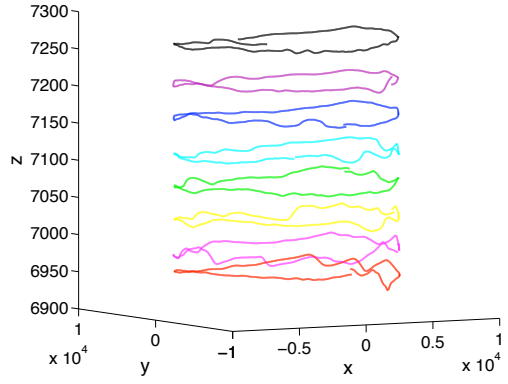


Figure 3. Eight passes encoded in different colors.

and height in a global ground plane coordinate system as z_G , if data is uniformly sampled in z_S , resolution ρ in the height dimension of the respective coordinate systems is given by

$$\rho_S = \frac{\lambda_c}{2\theta_{ext}} \text{ m} \quad \rho_G = \frac{\lambda_c \cos(\theta)}{2\theta_{ext}} \text{ m}, \quad (10)$$

and spatial aliasing in the height dimension occurs at

$$\text{Aliass} = \frac{\lambda_c}{2\Delta\theta} \text{ m} \quad \text{Alias}_G = \frac{\lambda_c \cos(\theta)}{2\Delta\theta} \text{ m}, \quad (11)$$

where θ_{ext} is the extent of the aperture in elevation angle. For the GOTCHA dataset, images formed using all 8 ideal passes, $\Delta\theta = 0.18^\circ$, $\theta_{ext} = 1.29^\circ$, and assuming a slant plane elevation of $\theta = 45^\circ$, have resolution in the height dimension of $\rho_S = 0.69$ m, and $\rho_G = 0.49$ m, and aliasing in the height dimension of $\text{Aliass} = 4.97$ m, and $\text{Alias}_G = 3.51$ m. We note that since the actual flight paths vary in elevation and are not uniformly sampled in height, the point spread function (PSF) of the SAR imager will not, in general, have a sinc-like structure. In this case, sidelobes of the PSF function may have non-negligible magnitude, and the uniform sampling resolution may not be sufficient to describe the image quality.

4. POLARIMETRIC PROCESSING AND 3D SHAPE ESTIMATION FROM MULTI-VIEW LAYOVER

Polarization diversity in radar has been shown to yield improved detection of targets in clutter.^{11, 12} Polarimetric measurements have also been used to characterize shape and orientation of the detected reflectors in the scene.¹³ GOTCHA data collection features a fully polarimetric sensor which measures the backscattered field with two linearly independent transmit and receive polarizations. These measurements can be combined into a scattering matrix S that maps the incident polarization state to the scattered polarization state. For the GOTCHA radar system with horizontal and vertical transmission diversity, the scattering matrix is given by

$$\begin{bmatrix} S_{hh} & S_{hv} \\ S_{vh} & S_{vv} \end{bmatrix} \quad (12)$$

where S_{ij} represents the complex gain that maps the j th incident polarization state to the i th scattered polarization state. We consider decomposition of the scattering matrix into a trihedral and dihedral basis:

$$S = a \begin{bmatrix} 1 & 0 \\ 0 & 1 \end{bmatrix} + b \begin{bmatrix} 1 & 0 \\ 0 & -1 \end{bmatrix} + c \begin{bmatrix} 0 & 1 \\ 1 & 0 \end{bmatrix} \quad (13)$$

where the first basis vector corresponds to the ideal trihedral response and the second and third basis vectors are chosen as the ideal dihedral responses for 0 and 45 degree tilt angles. We define the polarimetric feature ϕ as the angle between the trihedral and dihedral components:

$$\tan \phi = \frac{\sqrt{|b|^2 + |c|^2}}{|a|} \quad (14)$$

The polarimetric feature ϕ can be used to differentiate between odd and even-bounce scattering, with $\phi = 0$ corresponding to an ideal odd-bounce scattering mechanism and $\phi = \pi/2$ corresponding to an ideal even-bounce mechanism. For our preliminary study of the GOTCHA data we only considered calibration of the S_{hh} and S_{vv} channels using the GOTCHA scene calibration target tophat. For each pulse j we measured the phase angle between the complex returns $S_{hh}^j(r_{tophat})$ and $S_{vv}^j(r_{tophat})$ from the tophat reflector using:

$$c_j = \frac{S_{hh}^j(r_{tophat})S_{vv}^{j*}(r_{tophat})}{|S_{hh}^j(r_{tophat})S_{vv}^j(r_{tophat})|} \quad (15)$$

Then we applied polarimetric calibration to the S_{vv} channel for each pulse to introduce a 180 degrees phase differential between the co-pol polarimetric channels S_{hh} and S_{vv} :

$$S_{vv}^j[\text{cal}] = c_j e^{i\pi/2} S_{vv}^j[\text{uncal}] \quad (16)$$

The ϕ angle can be calculated for each pixel in the scene using the calibrated co-pol polarimetric measurements. The results on an image chip containing a passenger car are given in Figure 4(a). We observe that polarimetric feature can clearly differentiate between odd and even bounce mechanisms. Figure 4(b) shows the two main scattering mechanisms for a passenger car illuminated from the driver side: even bounce return from the side of the vehicle and the asphalt and odd bounce return from the curved surface at the top edge of the vehicle. The multiple view layover is clearly observed in this data – the odd bounce return from the top edge projects to a closer range than the double bounce return from the side of the vehicle – and we can hypothesize that the two returns should be colocated in ground plane coordinates x and y and then use the amount of layover to calculate the height z for each pixel corresponding the top edge of the vehicle. The results of this object based reasoning to recover shape from multi-view layover is given in Figure 5. We observe that the estimated shape provides rough information of the vehicle outline. The GOTCHA data set contains a polarimetric calibration array with dihedrals at various tilt angles. We are currently working on joint calibration of all four polarimetric channels and combining the polarimetric calibration with auto-focus processing to account for phase differences in the returns from the tophat calibration target.

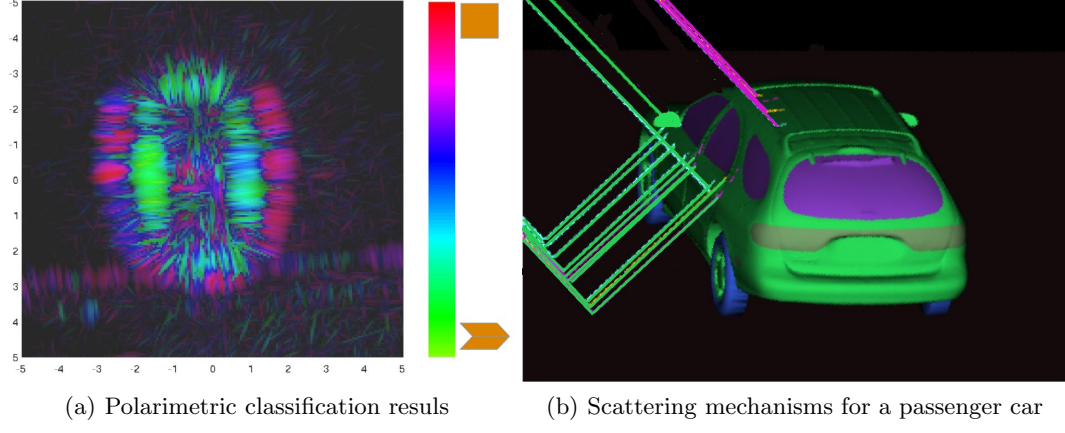


Figure 4. Polarimetric feature ϕ given in (14) classifies the returns from a passenger car into odd and even bounce scattering mechanisms.

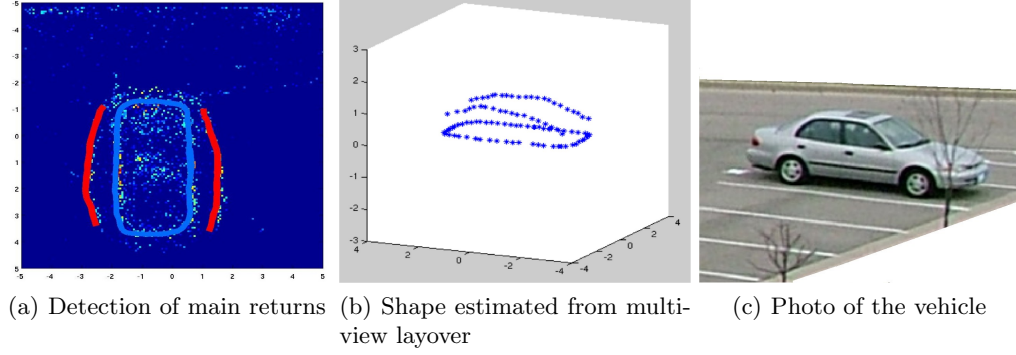


Figure 5. Three dimensional shape is estimated from multi-view layover using prior information about the spatial relation between the main scattering mechanisms

5. INTERFEROMETRIC SAR 3D RECONSTRUCTION

Interferometric SAR (IFSAR) is a method of sparse 3D image reconstruction, utilizing the phase difference between two SAR images formed at small differences in elevation angle to extract point scatterer heights.¹⁴ In this section, we discuss the application of IFSAR processing in reconstructing the GOTCHA scene calibration tophat.

Given two 2D images at two slightly different elevation angles, the height above pixel n at location (x_n, y_n) in a ground plane coordinate system is¹⁵ $z_n(x_n, y_n) = \frac{(\angle s_2 - \angle s_1)\lambda_c \cos(\theta_1)}{4\pi\Delta\theta}$, where the lowest elevation angle is denoted as θ_1 , and the difference in elevation angles is $\Delta\theta$; all elevation angles are assumed to be constant, and the phase of pixel n at elevation m is denoted as $\angle s_m$. This height estimate is derived for scattering centers that are well resolved. We also note that for phase defined to be in the range $[-\pi, \pi]$, the maximum unambiguous height range is controlled by $\Delta\theta$ and is given by

$$\left[\frac{-\lambda_c \cos(\theta_1)}{4\Delta\theta}, \frac{\lambda_c \cos(\theta_1)}{4\Delta\theta} \right]. \quad (17)$$

Scattering centers whose height is not contained within this interval will wrap into the interval. Small $\Delta\theta$ is desirable, since it results in large unambiguous range. For the GOTCHA data collection, $\Delta\theta = 0.21^\circ$ and angle $\theta = 45^\circ$ will give an unambiguous range of approximately 3m.

As discussed in Section 3, the elevation angle of each GOTCHA pass is not constant as a function of azimuth, implying that $\Delta\theta$ is not constant as a function of azimuth. To perform IFSAR processing, we first select an

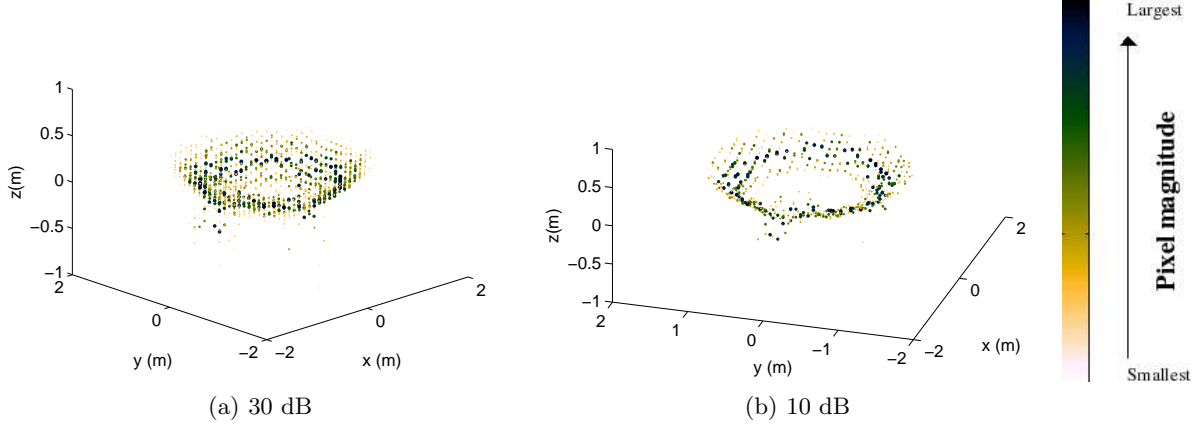


Figure 6. Ideal Tophat IFSAR reconstructions for different dB levels down from the maximum RCS pixel. Each reconstruction consists of 72 IFSAR reconstructions formed from 5° azimuth extent images with center azimuth angles $2.5^\circ:5^\circ:357.5^\circ$. All pixels that differ in more than a given dB level from the maximum RCS value of all pixels is discarded.

IFSAR image pair out of all possible 7 images pairs at elevation indices $(m, m+1)$, $m = 1, \dots, 7$ that has small variation in $\Delta\theta$ over an azimuth extent determined by the azimuth extent of the 2D SAR image, and on average, has small $\Delta\theta$. We select the IFSAR elevation pairs given our selection criterion by minimizing a uniformly weighted cost function of the normalized standard deviation and mean of $\Delta\theta$:

$$\operatorname{argmin}_{(\theta_m, \theta_{m+1})} \left(\frac{\operatorname{std}(\Delta\theta)}{\max \operatorname{std}(\Delta\theta)} + \frac{\operatorname{avg}(\Delta\theta)}{\max \operatorname{avg}(\Delta\theta)} \right). \quad (18)$$

The normalization terms, $\max \operatorname{std}(\Delta\theta)$ and $\max \operatorname{avg}(\Delta\theta)$ are maximized with respect to all IFSAR pairs $(m, m+1)$, $m = 1, \dots, 7$.

Reconstructed images of the tophat consist of its corner reflector and the sidelobes that result from the SAR imager, forming an annulus-like shape. Although elevation angle are not constant across the 5° azimuth extents used in image formation, the tophat reconstructions appear to be accurate.

6. 3D FILTERED BACKPROJECTION RECONSTRUCTION

In this section, we present 3D filtered backprojection reconstructions of a tophat and Ford Taurus station wagon from the GOTCHA scene using all eight passes of prominent point autofocus data.

Filtered backprojection is a tomographic image reconstruction method that inverts phase history data in the Fourier domain to generate an image in the spatial domain. The 2D backprojection algorithm commonly used in 2D SAR and medical imaging reconstructs a 2D planar image from projections of the image. First, each projection is transformed into the Fourier domain. Fourier transformed projections are then multiplied (filtered) by a linear ramp and Fourier inverted. Backprojection is then performed on each pixel in the 2D image plane, giving the reconstructed image. Backprojection is the process of finding the location where an image pixel projects onto a filtered projection line, adding the filtered projection value at this location to the pixel, and repeating the process over all filtered projection lines.¹⁶

Planar data collection and 2D filtered backprojection does not provide any resolution in the height dimension of the imaging plane. The 3D filtered backprojection algorithm is a generalization of 2D filtered backprojection that utilizes the volumetric phase history data collected at multiple elevation angles and is capable of resolving objects in the height dimension. The equation for 3D filtered backprojection image reconstruction is¹⁷

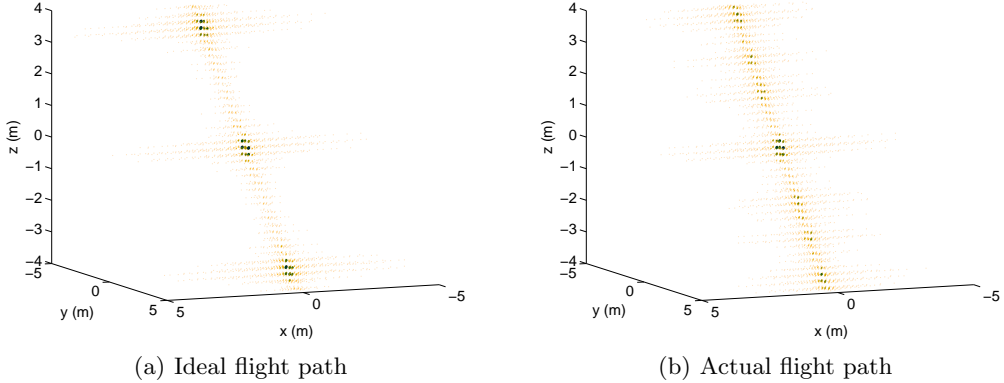


Figure 7. Point spread functions of a 3D filtered backprojection imager for ideal and actual radar flight paths. Images are formed using 8 elevation angles of GOTCHA data, a central azimuth angle of 92.5° , and azimuth extent of 5° .

$$\begin{aligned}
 u &= x \cos(\theta) \cos(\phi) + y \cos(\theta) \sin(\phi) + z \sin(\theta) \\
 Q_{\phi,\theta}(u) &= \int_{-\infty}^{\infty} P_{\phi,\theta}(U) |U^2 \cos(\theta)| e^{juU} dU \\
 s(x, y, z) &= \int_0^{2\pi} \int_0^{\frac{\pi}{2}} Q_{\phi,\theta}(u) d\theta d\phi. \tag{19}
 \end{aligned}$$

The value of u is the projection of the Cartesian ground plane coordinates onto the pointing vector from scene center to the radar at elevation angle θ and azimuth angle ϕ . Filtered projections are given by $Q_{\phi,\theta}(u)$, where $P_{\phi,\theta}(U)$ is the phase history line collected at aspect (ϕ, θ) . In both 2D and 3D cases, the filter is the Jacobian resulting from the change of coordinates in the Fourier domain from Cartesian to polar or spherical coordinates respectively; the 3D filter is quadratic for fixed elevation. This filter differs from the linear ramp filter used in 2D backprojection since the Jacobians used in changing to polar and spherical coordinates differ. The reconstructed pixel at Cartesian location (x, y, z) is given by $s(x, y, z)$. A discretization of the $s(x, y, z)$ equation in aspect (ϕ, θ) is simply the backprojection step in 2D backprojection, but in the 3D case, filtered projections do not necessarily lie in a reconstruction plane. All of the 3D filtered backprojection images presented here are generated by reconstructing planar slices of a 3D cube in a global ground coordinate system. The planar slices are orthogonal to the height dimension and are uniformly spaced in this dimension.

Figure 7(a) shows the PSF of a 3D filtered backprojection imager using the eight ideal GOTCHA elevation angles in Table 1 with a central azimuth angle of 92.5° and azimuth extent of 5° . The colormap encodes pixel magnitude and is the same as the one used in Figure 6. Figure 7(b) shows the PSF using the same central azimuth angle and extent, but the actual 8 GOTCHA flight paths, as shown in Figure 3. Resolution and aliasing in the height dimension in Figure 7(a) are predicted by equations (10) and (11) respectively. The actual flight path PSF in Figure 7(b) differs from the ideal PSF; it does not have sinc-like structure and exhibits high sidelobes which will degrade reconstructed images. The difference in PSFs is a result of the non-linear collection geometry of the actual flight path and the non-uniform sampling in elevation resulting from this geometry.

Reconstructed images of an ideal tophat and the tophat from the GOTCHA calibration scene using all eight elevation angle passes, a full 360° of azimuth extent, and the actual radar flight path are shown in Figure 8.

Lower RCS valued pixels are encoded in lighter, transparent colors and higher RCS pixels are encoded in darker, opaque colors. Prominent scattering from the corner of the tophat and sidelobe artifacts from the non-linear flight path are clearly visible in both the ideal and actual tophat. There are also some regions of dropout

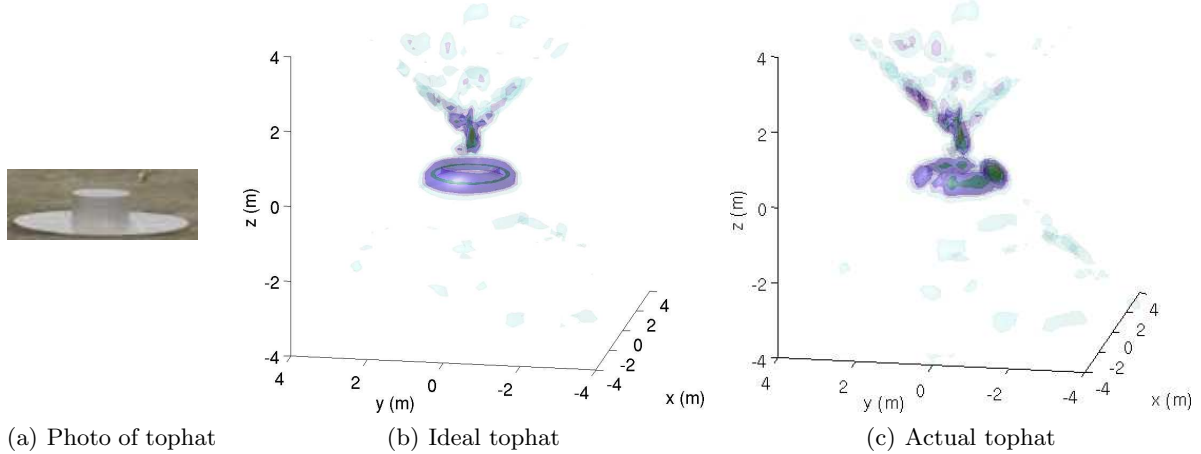


Figure 8. 3D filtered backprojection reconstructions and photo of the GOTCHA calibration tophat. Reconstructed images are formed using 8 elevation angles of GOTCHA data, a full 360° of azimuth extent, and the actual radar flight paths.

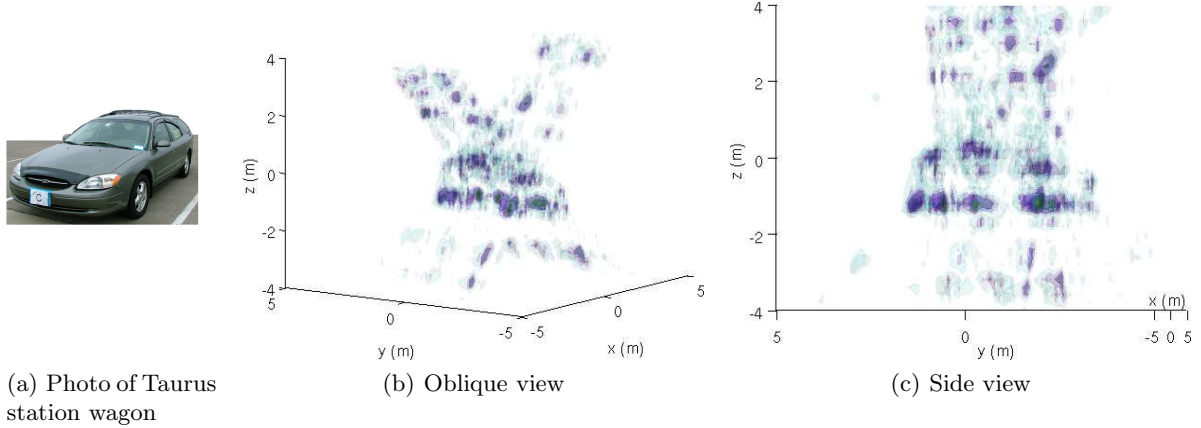


Figure 9. 3D filtered backprojection reconstructions and photo of a Taurus station wagon. Reconstructed images are formed using 8 elevation angles of GOTCHA data, and a full 360° of azimuth extent.

on the actual tophat that are not present on the ideal tophat; these dropouts may be from inaccuracies in autofocusing at certain aspect angles.

Figure 9 shows a reconstructed image of a Ford Taurus station wagon at two different aspect angles. The side of the car is parallel to the y axis in each subfigure, with the front of the car being at the most negative y value. The images show a profile of the car with the front portion of the car sloping up to the rear domed shape section of the car. Stronger returns from the bottom of the car appear to be from side panels or wheels, while low returns in the mid section of the car may be attributed to lack of reflection from glass windows. As in the tophat images, non-linear flight path imaging artifacts are present both above and below the car, degrading image quality.

7. MODEL BASED DECONVOLUTION FOR THREE DIMENSIONAL IMAGING

In this section we develop an approach to perform 3D model based deconvolution of the multipass GOTCHA data set. We use the scattering models developed by Rigling¹⁸ and later simplified to the monostatic case by Jackson and Moses.¹⁹ These models represent the object's expected scattering response of the incident radar pulse as a function of frequency, incident angles (azimuth and elevation), and the object dependent parameters

such as location, size, and orientation. The scattering models and the equations that represent their expected scattering behavior is derived by Jackson and Moses.¹⁹

The parameter f is the frequency and f_c is the carrier frequency while θ and ϕ are, respectively, the elevation (rotation from ground plane) and azimuth (rotation in the ground plane) angles of the radar. The object dependent parameters are denoted with a subscript m . The elevation angle is denoted by θ_m , the azimuth angle is denoted by ϕ_m , the yaw angle is denoted by ψ_m , and the length is denoted by L_m . Using these models, we represent the total scattering response as²⁰

$$T(f, \theta, \phi; \Theta) = \sum_m A_m S_m(f, \theta, \phi; \Theta_m) \exp \left\{ -\frac{j4\pi f}{c} \Delta R(\Theta_m) \right\} \quad (20)$$

where the m^{th} object's parameter vector is $\Theta_m = [\theta_m, \phi_m, \psi_m, L_m, x_m, y_m, z_m]$. The $\Delta R(\Theta_m)$ term in (20) is the difference in the distance between the radar and scene origin and the distance between the radar and the scatterer. Due to the approximate standoff distance of 9500m in the GOTCHA set, the far-field assumption does not always hold and so we use the more general near-field term

$$\Delta R(\Theta_m) = \underbrace{\sqrt{(x_m - x_0)^2 + (y_m - y_0)^2 + (z_m - z_0)^2}}_{\text{distance from radar to scene origin}} - \underbrace{\sqrt{(x_m - x_a)^2 + (y_m - y_a)^2 + (z_m - z_a)^2}}_{\text{distance from radar to scatterer}} \quad (21)$$

where terms subscripted with 0 are the coordinates of the scene center and terms subscripted with a are the coordinates of the radar antenna.

Our processing begins with a set of eight subaperture 2D ground plane images, one image for each elevation pass. Processing with a set of 2D images rather than one 3D image still preserves all of the information while reducing the computational complexity. The information is preserved because of the one-to-one correspondence between points from a single pass of phase history and the ground plane to which those points are projected. The complexity is reduced because we now work with a total image matrix of size $N \times N \times 8$ rather than $N \times N \times N$. We apply a watershed algorithm²¹ to segment features in the images. We use a single polarimetric channel and impose a particular scattering model for the model fitting instead of detecting the type. For a segmented feature, we form a set of templates by sampling its parameter vector. We do this by sampling Θ_m and forming eight 2D ground plane images by emulating the GOTCHA flight path (i.e. range, azimuth, elevation) and data collection information (i.e. frequency, bandwidth). We correlate this template set against the segmented feature to determine initialization points.

Formally, we have a segmented feature across all eight images. We take the pixels of interest from all eight images and stack them into a vector, Y_m . We use those same pixel indices from Y_m to extract pixels from the image templates and form a set of vector templates $X(\Theta_{m,i})$ with $i = \{1, \dots, K\}$ indexing the templates. The maximum likelihood estimate, with an equal energy constraint on all templates, in additive white Gaussian noise yields

$$\hat{\Theta}_{m,i} = \arg \max_{\Theta_{m,i}} \operatorname{Re}\{Y_m^H X(\Theta_{m,i})\} \quad (22)$$

where superscript H denotes the conjugate transpose. We deviate a bit from this and instead score correlation as

$$\hat{\Theta}_{m,i} = \arg \max_{\Theta_{m,i}} \operatorname{abs}\{Y_m^H X(\Theta_{m,i})\} \quad (23)$$

The change from $\operatorname{Re}\{\cdot\}$ to $\operatorname{abs}\{\cdot\}$ is done to accomodate for the unknown constant phase remaining from the motion compensation processing. Due to the ‘pseudo-aliasing’ of features resulting from the GOTCHA elevation angle sampling structure, we use the top scoring template and the next highest scoring template that has a different height parameter z_m as initialization points in our multistart simplex-search optimization stage using the Matlab *fminunc* command.

The optimization routine runs similarly as the initialization procedure in that we form eight 2D ground plane images from the estimated parameter vector and GOTCHA information. However, we modify the cost function

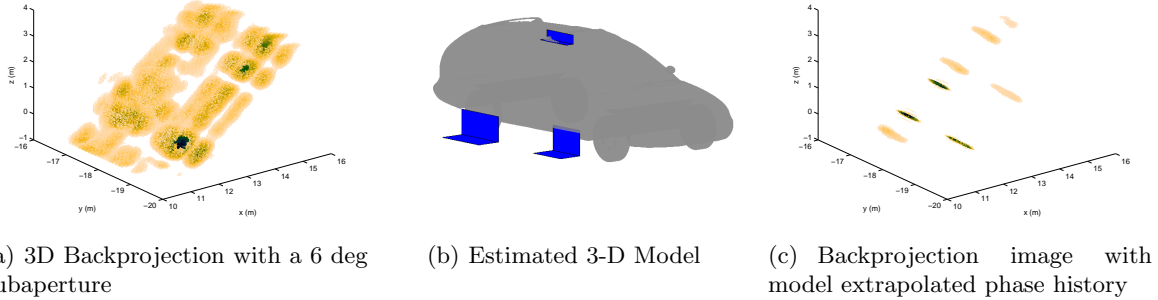


Figure 10. Model based deconvolution for three dimensional target reconstruction

in (23) to account for the energy of the estimate, resulting in

$$\hat{\Theta}_m = \arg \min_{\Theta_m} -\frac{\text{abs}\{Y_m^H X(\Theta_m)\}}{\sqrt{X^H(\Theta_m) X(\Theta_m)}} \quad (24)$$

In the case of multistart, the parameter vector associated with the lower cost is the one we choose. We conduct this template creation and optimization procedure in parallel for all segmented features.

We apply our approach to a $10\text{m} \times 10\text{m}$ scene in the GOTCHA data containing a single vehicle. Figure 10 (a) shows a 3D backprojection image of the scene formed using six degree subapertures from all eight passes. The aperture is centered broadside to the vehicle in the scene. Notice the ambiguity along the axis perpendicular to the radar line of sight. Figure 10 (b) shows our estimated dihedrals placed on a CAD model of the vehicle. Figure 10 (c) shows a 3D backprojection image after the application of our algorithm. We fit three dihedrals to explain the scattering behavior. After we estimate the parameters, we extrapolate in phase history by using 2Ghz bandwidth and 50 evenly spaced samples over 20° elevation.

8. CONCLUSION

In this paper we considered 3D imaging with circular SAR. We reviewed three dimensional imaging methods for CSAR data; illustrated these methods using computed examples from the GOTCHA data set, and introduced new algorithms for CSAR processing for three dimensional target reconstruction. A promising area for future work is the design of automatic target recognition algorithms and target models for wide-angle three dimensional imaging systems.

ACKNOWLEDGEMENT

This material is based upon work supported by the Air Force Office of Scientific Research under Award No. FA9550-06-1-0324 and in part by Air AFRL/SNAS under agreement number FA8650-04-1-1721 (BAA 04-03-SNK Amendment 3). Any opinions, findings, and conclusions or recommendations expressed in this publication are those of the authors and do not necessarily reflect the views of the Air Force. We also would like to acknowledge support from SET corporation for Mr. Austin's summer internship, resulting in some of the results presented here.

REFERENCES

1. C. H. Casteel, L. A. Gorham, M. J. Minardi, S. Scarborough, and K. D. Naidu, "A challenge problem for 2D/3D imaging of targets from a volumetric data set in an urban environment," in *Proc. SPIE 6568*, E. G. Zelnio and F. D. Garber, eds., Apr 2007.
2. M. Y. Jin and M. Chen, "Analysis and simulation for a spotlight-mode aircraft SAR in circular flight path," in *Proceedings of IGARSS 93*, **1**, Aug 1993.
3. M. Soumekh, "Reconnaissance with slant plane circular SAR imaging," *IEEE Trans. Image Processing* **5**, Aug 1996.

4. D. E. Dudgeon, R. T. Lacoss, C. H. Lazott, and J. G. Verly, "Use of persistant scatterers for model-based recognition," in *Proc. SPIE 2230*, pp. 356–368, April 1994.
5. L. C. Trintinalia, R. Bhalla, and H. Ling, "Scattering center parameterization of wide-angle backscattered data using adaptive Gaussian representation," *IEEE Trans. Antennas and Propagation* **45**, pp. 1664–1668, Nov 1997.
6. M. Soumekh, *Synthetic Aperture Radar Signal Processing with MATLAB Algorithms*, Wiley, 1999.
7. C. V. Jakowatz and P. A. Thompson, "A new look at spotlight mode synthetic aperture radar as tomography: imaging 3D targets," *IEEE Trans. Image Processing* **4**, May 1995.
8. L. J. Moore and L. C. Potter, "Three-dimensional resolution for circular synthetic aperture radar," in *Proc. SPIE 6568*, E. G. Zelnio and F. D. Garber, eds., Apr 2007.
9. R. L. Moses and M. Cetin, "Wide angle SAR imaging," in *Proc. SPIE 5427*, E. G. Zelnio and F. D. Garber, eds., Apr 2004.
10. R. L. Moses and L. C. Potter, "Noncoherent 2D and 3D SAR reconstruction from wide-angle measurements," in *13th Annual Adaptive Sensor Array Processing Workshop*, MIT Lincoln Laboratory, (Lexington, MA), June 2005.
11. R. L. Dilksavor, *Detection of target scattering centers in terrain clutter using an ultra-wideband, fully-polarimetric synthetic aperture radar*. PhD thesis, The Ohio State University, 1993.
12. V. Larson and L. Novak, "Polarimetric subspace target detector for SAR data based on the huynen dihedral model," in *Proceedings of the SPIE International Symposium on Algorithms for Synthetic Aperture Radar Imagery II*, D. A. Giglio, ed., **2487**, pp. 235–250, (Orlando, FL), Apr 1995.
13. E. Ertin and L. C. Potter, "Polarimetric classification of scattering centers," *IEEE Trans. on AES* **36**, pp. 738–749, July 2000.
14. C. D. Austin and R. L. Moses, "Interferometric synthetic aperture radar detection and estimation based 3D image reconstruction," in *Algorithms for Synthetic Aperture Radar Imagery XIII*, SPIE Defense and Security Symposium, (Orlando, FL), 17-21 April 2006.
15. C. V. Jakowatz Jr., D. E. Wahl, P. H. Eichel, D. C. Ghiglia, and P. A. Thompson, *Spotlight-Mode Synthetic Aperture Radar: A Signal Processing Approach*, Kluwer Academic Publishers, Boston, 1996.
16. A. Jain, *Fundamentals of Digital Image Processing*, Prentice Hall, 1988.
17. K. Knaell and G. Cardillo, "Radar tomography for the generation of three-dimensional images," *IEE Proceedings-Radar, Sonar and Navigation* **142**, pp. 54–60, April 1995.
18. B. D. Rigling, *Signal Processing Strategies for Bistatic Synthetic Aperture Radar*. PhD thesis, The Ohio State University, 2003.
19. J. A. Jackson and R. L. Moses, "Feature extraction algorithm for 3D scene modeling and visualization using monostatic SAR," in *Algorithms for Synthetic Aperture Radar Imagery XIII*, E. G. Zelnio and F. D. Garber, eds., *Proceedings of SPIE* **6237**, May 2006.
20. L. C. Potter and R. L. Moses, "Attributed scattering centers for SAR ATR," *IEEE Transactions on Image Processing* , 1997.
21. M. Koets, "Automated algorithms for extraction of physically relevant features from synthetic aperture radar imagery," Master's thesis, The Ohio State University, 1998.